The International Journal of Advanced Manufacturing Technology (2020) 107:4191–4200
https://doi.org/10.1007/s00170-020-05309-7

ORIGINAL ARTICLE

Effect of temperature buildup on milling forces in additive/subtractive hybrid manufacturing of Ti-6Al-4V

Shuai Li[1,2] · Bi Zhang[1] · Qian Bai[3]

Received: 18 November 2019 / Accepted: 7 April 2020 / Published online: 25 April 2020

Abstract
An additive/subtractive hybrid manufacturing (ASHM) combines the advantages of both additive and subtractive processes for fabricating complex parts of a better quality. While in an additive manufacturing process, temperature buildup is fast because of heat accumulation from a laser or electron beam, which exerts a great influence on the successive subtractive process. This study firstly measures the temperature variation of a Ti-6Al-4V workpiece in the direct material deposition (DMD) process, and then designs a heating device for a milling experiment at elevated temperatures. The effect of temperature buildup on milling forces is investigated through the experiment and a 2D thermal-mechanical coupling model. For work hardening effect and rapid tool wear, the milling forces are hardly decreased when the preheating temperature is lower than 300 °C. At a preheating temperature of 300 °C or higher, a significant reduction in milling forces is recorded, which may be attributed to the thermal softening effect on the workpiece material. The decreasing trend is more obvious at a larger feed-per-tooth. The thermal softening effect is reflected in the deformation layer in the subsurface of the machined workpiece. The study provides a guide to the determination of ASHM process parameters for Ti-6Al-4V.

Keywords Additive/subtractive hybrid manufacturing · Temperature buildup · Ti-6Al-4V · Milling forces · Subsurface

1 Introduction

Additive manufacturing (AM) offers great benefits of manufacturing parts with geometric complexities efficiently. It realizes "near-net-shaped manufacturing" from a CAD model to a final part, which greatly reduces material waste and saves energy [1–3]. An AMed titanium alloy has many applications [4]. However, an AMed Ti-6Al-4V workpiece has poor geometric and dimensional accuracies as well as poor surface finish due to "step-effect" and partially melted powders on the surface [5, 6]. To solve these problems, the additive/subtractive hybrid manufacturing (ASHM) has been put forward by some scholars, as shown in Fig. 1, in which the machining process can remove the rough layer from the surface of a workpiece and maintain both geometric and dimensional accuracies [7–9].

Xiong et al. [10] presented a new metal direct rapid prototyping approach, i.e., hybrid plasma deposition and milling, to ensure high dimensional accuracy of a deposited workpiece. Ye et al. [11] combined direct metal deposition (DMD) and high-speed milling together and developed a hybrid additive manufacturing machine tool. The high-speed milling removed the rough layer and improved the surface quality. Du et al. [12] studied a novel method of ASHM for the 18Ni maraging steel and found that the surface morphology of an ASHMed workpiece was better than that of the workpiece fabricated by using the selective laser melting (SLM). However, in the ASHM process, temperature buildup caused by laser exerts a great influence on successive machining processes in terms of tool wear, milling forces, and surface integrity, especially for Ti-6Al-4V with low thermal conductivity [13]. Therefore, it is necessary to study the effect of the AM-resulted temperature on subtractive processes in ASHM.

Machining characteristics of Ti-6Al-4V wrought workpiece at high temperature were studied in the thermally

✉ Bi Zhang
zhangb@sustech.edu.cn

[1] Department of Mechanical and Energy Engineering, Southern University of Science and Technology, Shenzhen 518055, China

[2] School of Mechatronics Engineering, Harbin Institute of Technology, Harbin 150001, China

[3] Key Laboratory for Precision and Non-traditional Machining Technology of Ministry of Education, Dalian University of Technology, Dalian 116024, China

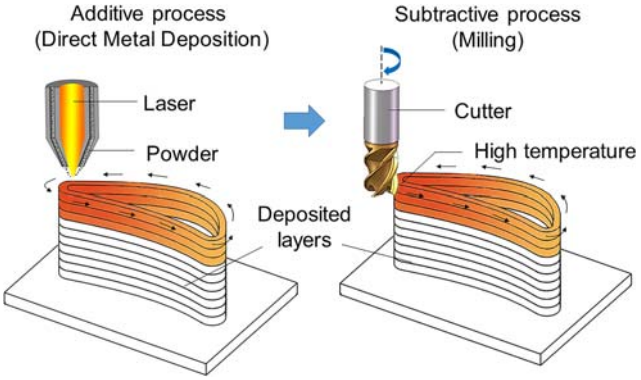

Fig. 1 Additive and subtractive hybrid manufacturing process

assisted machining. Ginta et al. [14] preheated Ti-6Al-4V workpiece by an induction coil to study machinability of the material. The milling forces and vibrations of the preheated machining were found lower than those in the conventional machining. In laser-assisted machining (LAM), cutting forces and tool wear at different laser powers were investigated by Dandekar et al. [15]. They found that the optimum preheated temperature in cutting zone was 250 °C, at which tool life was increased by 70%, whereas surface roughness was reduced by 30% as compared with the conventional machining. Sun et al. [16–18] carried out a series of cutting experiments to investigate the machinability of titanium alloy in LAM and reported that both cutting forces and tool wear were reduced with the increase of laser power. A higher temperature always contributed to the improvement of titanium machinability. However, Hedberg et al. [19] found that for the Ti-6Al-4V workpiece in LAM, milling forces were hardly reduced when the average material temperature was at 200 °C and 250 °C, but reduced at higher temperatures. In LAM, the softening effect on the machined material in the cutting zone by local heating is considered as the key factor to cause the cutting force reduction and tool life improvement. While in ASHM, the whole workpiece is heated, which results in a temperature field different from that in local heating. The difference in the temperature fields may have a distinct effect on the milling processes.

This study investigates the effect of temperature buildup on milling forces of the AMed Ti-6Al-4V in the ASHM process. Firstly, the temperature buildup after additive process in the DMD is measured to determine the temperature range before machining process. Then, a heating device is designed to conduct milling experiments at specific temperatures. Milling forces are recorded and peak forces are analyzed at different temperatures and feed-per-tooths. Tool wear and subsurface deformation layer of the machined surface are observed. Furthermore, a two-dimensional (2D) finite element model based on DEFORM V11.0 is built to study thermal-mechanical mechanism at specific preheating temperatures. The thermal softening effect on the machined material is analyzed in combination with the model and subsurface deformation layer.

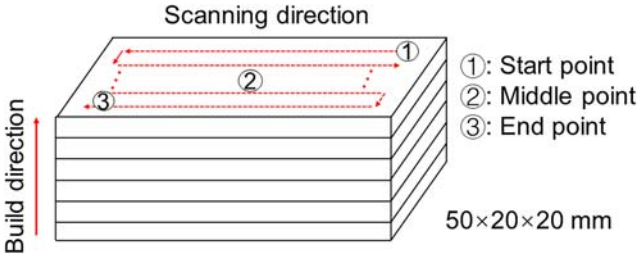

Fig. 2 Measurement of AM-resulted temperature buildup in the DMD process

2 Experimental setup and methodology

2.1 Temperature buildup measurement in additive process

In the practical ASHM process, the AM-resulted temperature increase varies due to the heating and cooling cycles, thus it is difficult to study the effect of temperature on machinability in the ASHM process. To investigate the influence of a specific temperature on machinability of AMed Ti-6Al-4V in the machining process, temperature variation in the DMD process was measured firstly. Then, a heating device was set on a CNC machine to maintain a constant temperature during milling. Therefore, machinability of AMed Ti-6Al-4V was studied at a specific temperature.

The additive manufacturing process was conducted on a KUKA robot, with a 2.5-kW Nd:YAG laser. A workpiece with dimensions of 50 × 20 × 20 mm was fabricated by using Ti-6Al-4V powders with an average diameter of 90 μm. In the DMD process, the laser power was 1000 W, the laser scanning speed was 15 mm/min, the rotation speed of the powder feeder was 15 rev/min, the overlap of laser track was 40%, the hatch spacing was 1.2 mm, and 60 layers were deposited in total. The "zigzag" scanning strategy was adopted, as shown in Fig. 2. Since tool exchanging time between an additive manufacturing process and a machining process was measured as around 20 s in ASHM, the temperature after 20-s cooling time was recorded by thermocouples at three measuring locations (start, middle, and end points of the laser track), as shown in Fig. 2. Therefore,

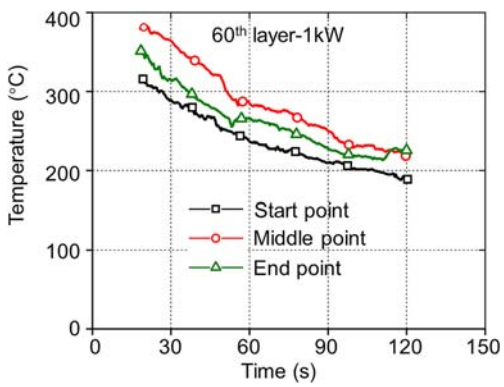

Fig. 3 Temperature variation after the DMD process

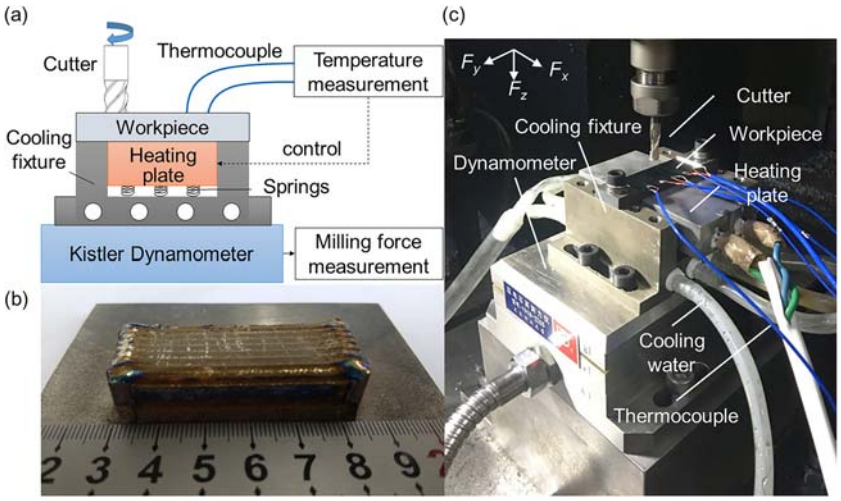

Fig. 4 Experiment setup. **a** Diagram of the setup. **b** DMDed workpiece. **c** Milling experiment platform

the AM-resulted temperature buildup of Ti-6Al-4V workpiece was obtained, which can be considered as the initial condition for the successive milling process.

Temperature variation within 20 s to 120 s after the additive manufacturing process is shown in Fig. 3. The highest temperature was around 380 °C at the middle point in 20 s after deposition. Temperature at the middle point was generally higher than those at the start and end points during the cooling cycle, due to the different heat dissipation condition. The heat dissipation condition was poor at the middle point, which was surrounded by Ti-6Al-4V of low thermal conductivity. Temperatures at the three measuring points declined with cooling time and dropped slowly to 200 °C after 120 s, during which the milling operation could be completed. Thus, subsequent dry milling experiments could be conducted at temperature from 200 °C to 380 °C in the CNC machine with a heating device. For comparison, dry milling experiments at room temperature were also conducted.

2.2 Milling experiment setup and parameters

In order to carry out milling experiments of the DMDed workpiece at a specific temperature, a heating device was designed and set on a NHX650 high-speed milling machine. The diagram of the device is shown in Fig. 4(a): a heating plate was placed beneath the workpiece to simulate the AM-resulted temperature increase, and a force dynamometer (Kistler YDCB-III05) was used to record milling forces. Protecting heat effect on the dynamometer, a water-cooling fixture was placed between the heating plate and the dynamometer. Several thermocouples were welded on the workpiece surface to accurately control the preheating temperature before the milling operation. The DMDed workpiece is shown in Fig. 4(b). Before the experiments, the coarse top layer was removed to avoid the potential influence of an oxidation layer. A TiAlN-coated two-flute carbide end mill with a diameter of 6 mm and a helix angle of 30° was used. The experimental platform is shown in Fig. 4(c).

Six sets of slot-milling experiments at 24 °C (room temperature), 200 °C, 250 °C, 300 °C, 340 °C, and 380 °C were conducted at a series of feed-per-tooths, 0.05 mm/z, 0.07 mm/z, 0.09 mm/z, 0.11 mm/z, 0.13 mm/z, successively. The experimental parameters are listed in Table 1.

3 Finite element simulation model

3.1 Geometric modeling and initial conditions

The commercial software DEFORM V11.0 was used to develop a 2D thermal-mechanical coupling simulation model for the slot milling at different temperatures. The helix angle of

Table 1 Experimental parameters

No.	Rotation n (r/min)	Axial cutting depth a_p (mm)	Preheating temperature T (°C)	Feed-per-tooth f_z (mm/z)
1	4000	0.6	24	0.05, 0.07, 0.09, 0.11, 0.13
2	4000	0.6	200	0.05, 0.07, 0.09, 0.11, 0.13
3	4000	0.6	250	0.05, 0.07, 0.09, 0.11, 0.13
4	4000	0.6	300	0.05, 0.07, 0.09, 0.11, 0.13
5	4000	0.6	340	0.05, 0.07, 0.09, 0.11, 0.13
6	4000	0.6	380	0.05, 0.07, 0.09, 0.11, 0.13

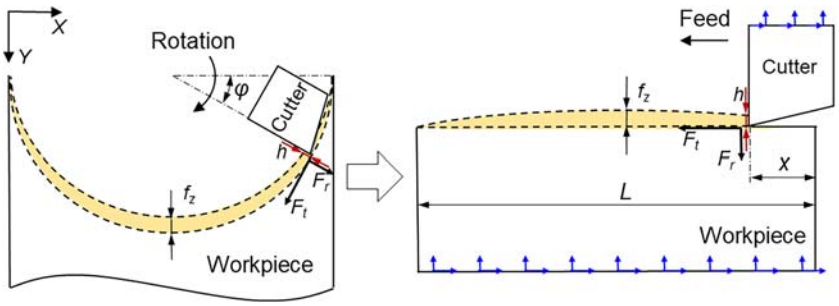

Fig. 5 Simplification of milling to orthogonal cutting

the milling cutter was not considered due to a flat section at the cutter tip. Milling force in the *Z* direction was ignored due to a small axial cutting depth. Thus, the milling process could be simplified as the 2D orthogonal cutting, which can reduce the number of elements and improve the computational efficiency [20]. As shown in Fig. 5, the slot-milling model was converted to an orthogonal cutting model by transforming uncut chip geometry based on the uncut chip thickness formula (Eq. (1)).

$$\begin{cases} h = f_z \cdot \sin\varphi \\ \varphi = \dfrac{x}{R} \end{cases} \tag{1}$$

where f_z is the feed-per-tooth and φ is the rotation angle and approximately equal to the ratio of the swept arc of tool tip x and tool radius R (x/R). Uncut chip thickness changes with rotation of milling cutter and reaches the maximum (f_z) at half cutting length. The cutter was set as a rigid body with its rake and clearance angles at 0° and 10°, respectively. The value of the cutting-edge radius was 0.02 mm.

As shown in Fig. 5, cutting length L in the orthogonal cutting model equals to half the circumference of the cutter. Freedoms of the workpiece were restricted in the vertical directions along the bottom line. The workpiece moved along the horizontal direction at a speed of 76 m/min, which was equal to the circumferential speed of the cutter of 6-mm diameter rotating at 4000 rpm. Freedoms of the cutter were restricted in all the directions. The workpiece and cutter were discretized with quadrilateral elements. Mesh density windows were applied to the cutting area of the workpiece and cutter tip to refine the mesh.

3.2 Johnson-Cook constitutive model and material properties

The AMed Ti-6Al-4V has the Widmanstatten microstructure with a tensile strength reportedly comparable to the wrought one [21, 22]. There is hardly a clear distinction between the AMed Ti-6Al-4V workpiece and wrought workpiece in terms of machining forces [23, 24]. Thus, in this study, material properties of the wrought Ti-6Al-4V are adopted in the finite element (FE) model. The Johnson-Cook constitutive model, expressed in Eq. (2), is adopted to determine the flow stress considering the factors of strain, strain rate, and temperature [25]. Where $\overline{\sigma}$ and $\overline{\varepsilon}$ are equivalent stress and plastic strain, $\dot{\overline{\varepsilon}}$ and $\dot{\overline{\varepsilon}}_0$ are equivalent and reference strain rate. A, B, C, m, and n are the initial yield stress, the hardening modulus, the thermal softening coefficient, and the strain rate-dependent coefficient, respectively. T, T_{room}, and T_{melt} are the workpiece temperature, the melting temperature of material, and the room temperature, respectively.

$$\overline{\sigma} = \left[A + B\left(\overline{\varepsilon}\right)^n\right]\left[1 + C\ln\left(\frac{\dot{\overline{\varepsilon}}}{\dot{\overline{\varepsilon}}_0}\right)\right]\left[1-\left(\frac{T-T_{\text{room}}}{T_{\text{melt}}-T_{\text{room}}}\right)^m\right] \tag{2}$$

The parameters in the Johnson-Cook constitutive model of Ti-6Al-4V are specified in Table 2. The cutter material is tungsten carbide. Temperature-dependent physical and mechanical properties of the workpiece and cutter are shown in Table 3.

The heat transfer coefficient between the cutter and workpiece was set as 10^7 kW m^{-2} K^{-1} to accelerate temperature rise of the cutter [27, 28]. The ambient temperature was set as 24 °C, and the initial temperature of the workpiece was set at different levels of 24 °C, 200 °C, 250 °C, 300 °C, 340 °C, and 380 °C, in consistence with the respective preheating temperatures in the experiment. A hybrid friction model was used in DEFORM 11.0 to describe the sticking contact and the sliding contact [29, 30]. The separation of the two areas is defined in Eq. (3),

$$\begin{cases} sticking \;\; \tau_f = mk \;\; \mu p \geq mk \\ sliding \;\; \tau_f = \mu p \;\; \mu p < mk \end{cases} \tag{3}$$

where τ_f is frictional stress, p is interface pressure, k is the shear yield stress of the workpiece, m is the shear friction factor in sticking region and was set to 0.7 in this study, and the Coulomb friction factor μ was set to 0.3 [31, 32].

Table 2 Johnson-Cook constitutive model parameters of Ti-6Al-4V [25]

A (MPa)	B (MPa)	C	m	n
860	683.1	0.035	1	0.47

Table 3 Physical and mechanical properties of workpiece and cutter materials

Parameters	Workpiece (Ti-6Al-4V) [25]	Cutter (tungsten carbide) [26]
Density (kg m^{-3})	4430	11,900
Poisson's ratio	0.34	0.22
Elastic modulus (GPa)	109 (50 °C) 91 (250 °C) 75 (450 °C)	650
Thermal conductivity (W m^{-1} $°C^{-1}$)	6.8 (20 °C)	40.15 (100 °C)
	7.4 (100 °C)	48.55 (300 °C)
	9.8 (300 °C)	56.95 (500 °C)
	11.8 (500 °C)	65.35 (700 °C)
Heat capacity (N mm^{-2} $°C^{-1}$)	2.71 (20 °C)	4.12 (100 °C)
	2.76 (100 °C)	4.40 (300 °C)
	2.99 (300 °C)	4.69 (500 °C)
	3.11 (500 °C)	4.97 (700 °C)
Thermal expansion (mm^{-1} K^{-1})	8.6×10^{-6}	4.7×10^{-6}

Serrated chips are most often generated in the cutting process for Ti-6Al-4V. Fracture criteria should be established to simulate ductile fracture in the serrated chip formation process. In this study, the normalized Cockroft and Latham damage equation is adopted as follows:

$$C=\int_0^{\bar{\varepsilon}_f} \frac{\boldsymbol{\sigma}^*}{\overline{\boldsymbol{\sigma}}} d\bar{\varepsilon} \tag{4}$$

where $\bar{\varepsilon}_f$ is the equivalent fracture strain, $\boldsymbol{\sigma}^*$ is the maximum principal stress, $\overline{\boldsymbol{\sigma}}$ is the equivalent stress, and C is the fracture threshold. The critical fracture threshold is considered as a constant 0.177 according to [33, 34].

4 Results and discussion

4.1 Effect of temperature on milling forces

Milling forces in the X and Y directions were extracted from the data recorded in the experiment and compared with the simulation results. Because the milling process was simplified to the orthogonal cutting in the FE model, Eq. (4) was used to convert the tangential force F_t and radial force F_r to milling forces in the X and Y directions.

$$\begin{cases} F_x = -\cos\varphi \cdot F_t - \sin\varphi \cdot F_r \\ F_y = \sin\varphi \cdot F_t - \cos\varphi \cdot F_r \end{cases} \tag{5}$$

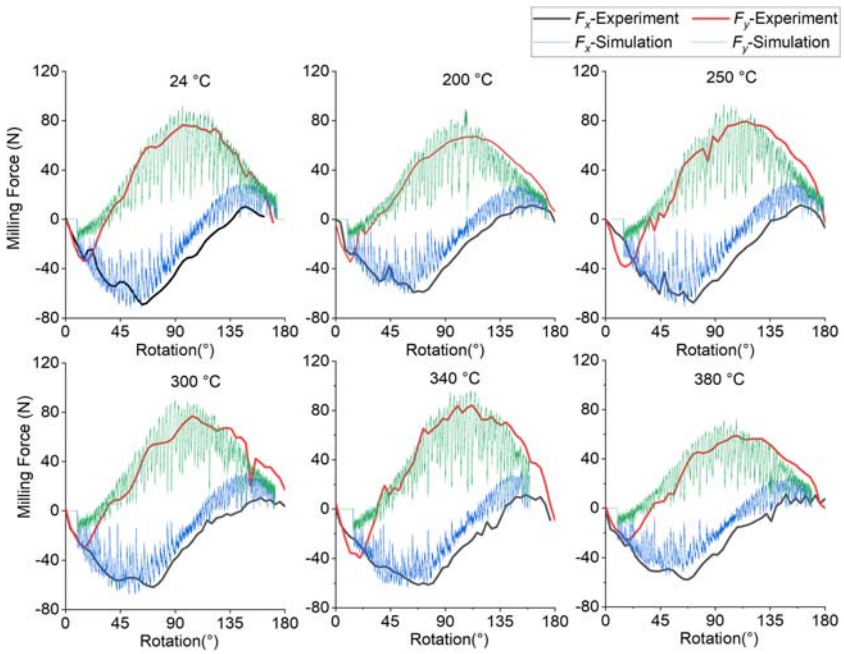

Fig. 6 Comparison of experimental and simulational milling force profiles at various preheating temperatures for f_z = 0.05 mm/z

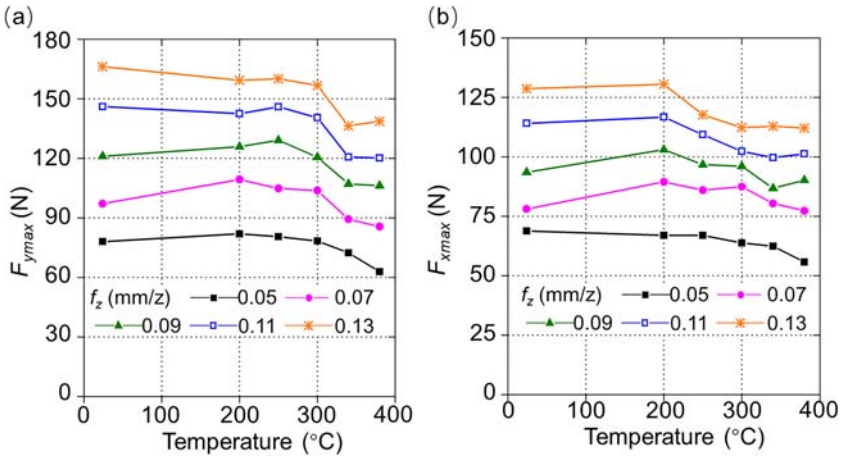

Fig. 7 Peak forces vs. preheating temperatures and feed-per-tooths. **a** F_{ymax}. **b** F_{xmax}

Each set of the experiment was conducted at a specific temperature with a series of feed-per-tooths. The profiles of the experimental and simulational milling forces are compared at $f_z = 0.05$ mm/z in Fig. 6. The milling forces change with the rotation of the cutter, and wave profiles of both the experimental and simulational milling forces were close, which justifies the simulation model. However, simulational milling forces were generally smaller than the experimental forces in all cases. One of the reasons for the discrepancy is that tool wear was ignored in the simulation, resulting in a reduced radial force F_r. Preheating the workpiece could cause faster tool wear, which will be discussed later. Another reason is that as the AMed Ti-6Al-4V material was produced from the additive manufacturing process, its material parameters might be different from the book values normally used for Ti-6Al-4V.

Comparing the peak forces of the milling force profiles in the X and Y directions, an obvious trend could be observed with increasing preheating temperature. Experimental peak forces in the X and Y directions, F_{xmax} and F_{ymax}, at various preheating temperatures and feed-per-tooths were extracted from the recorded data. The result is shown in Fig. 7 with only the peak forces.

F_{ymax} did not show much decrease when the preheating temperature was lower than 300 °C. The same phenomenon can be observed in Fig. 7(b) on F_{xmax} at a small feed-per-tooth. When the preheating temperature was higher than 300 °C, the peak forces were decreased markedly by 19.0% and 19.5% respectively for F_{ymax} and F_{xmax} at 380 °C when $f_z = 0.05$ mm/z. With an increase in f_z from 0.05 to 0.13 mm/z, the decreasing trend of the peak forces became more obvious, 17.9% and 12.3% respectively for F_{ymax} and F_{xmax} at 340 °C when $f_z = 0.13$ mm/z, but only 7.24% and 9.3% when $f_z =$ 0.05 mm/z.

4.2 Temperature increase and thermal softening effect

The variation in the peak forces in milling is associated with work hardening and thermal softening effects. The thermal softening effect can reduce flow stress and cutting force [18]. Figure 8 shows the relationship between the temperature and flow stress of Ti-6Al-4V at a strain of 0.2 [35]. The flow stress linearly decreases with the increase of temperature, which indicates a significant thermal softening effect on the workpiece material. For temperature buildup in ASHM, cutting temperature will be higher than that at room temperature. Thus, the thermal softening effect may overtake the work hardening effect on the workpiece material. In order to provide an insight into the thermal effect on a machined workpiece, both temperature and effective stress in the cutting zone were investigated in the FE model.

Figure 9 shows temperature fields and the highest temperature in the cutting zone at various preheating temperatures when uncut chip thickness reached f_z. The highest temperature was near the zone close to the tool tip. As shown in Fig. 9, the highest temperature increases from 687 to 802 °C as preheating temperature reached to 380 °C. The highest cutting temperature increases with preheating temperature at a near-linear trend. Thus, more significant thermal softening effect is expected with a higher preheating temperature, causing a further reduction in material strength.

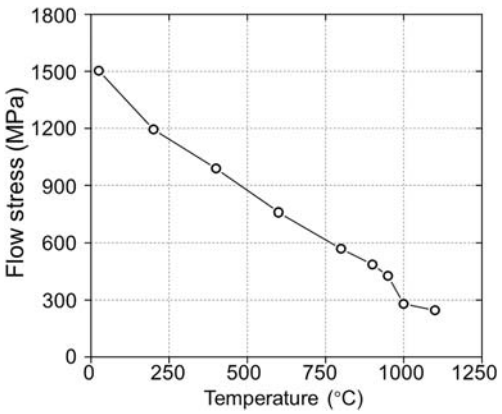

Fig. 8 Relationship between temperature and flow stress of Ti-6Al-4V [35]

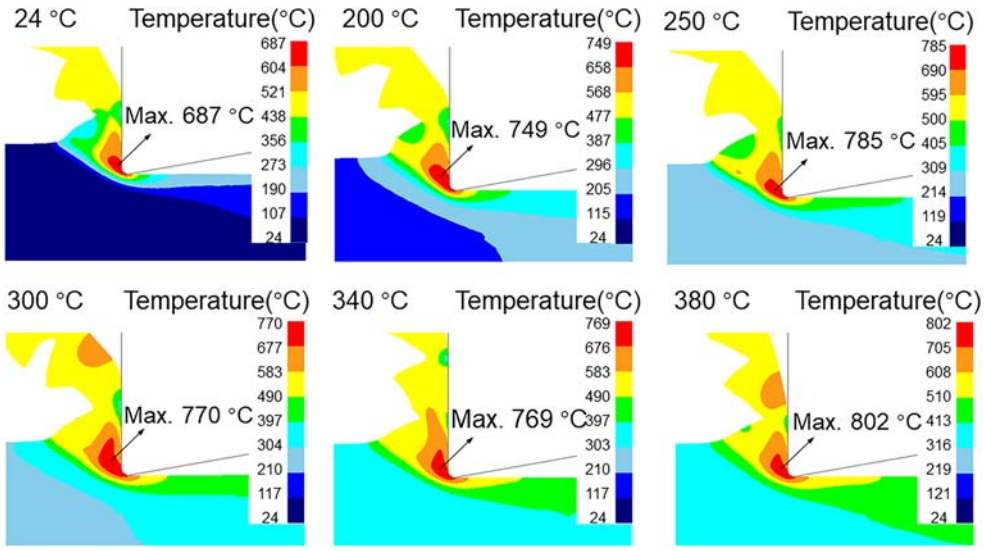

Fig. 9 Temperature fields in simulation when $f_z = 0.05$ mm/z

Figure 10 shows the effective stress distribution in the cutting zone at various preheating temperatures. High effective stress is concentrated in the primary and secondary cutting zones. As preheating temperature increases from room temperature to 380 °C, the maximum effective stress in the primary zone drops from 1536 to 1185 MPa. The results are consistent with [36]. A significant reduction in the effective stress is found in simulations.

Enhanced thermal softening effect on workpiece material at preheating temperature can be demonstrated by the simulation results. The cutting temperature increases with preheating temperature and reduces the effective stress in the cutting zone. Therefore, the significant reduction in milling forces at a preheating temperature of 300 °C or higher can be attributed to the thermal softening effect of the workpiece material. At a preheating temperature lower than 300 °C, the work hardening effect counteracts the thermal softening effect on the workpiece material. In this case, milling forces hardly decrease. With an increase in feed-per-tooth, the decreasing trend of the peak forces is more obvious. This phenomenon is attributed to the increased cutting heat produced in the cutting process. An increased cutting heat causes a higher temperature rise in the cutting zone. Thus, the thermal softening effect may overtake the work hardening effect at a lower preheating temperature, leading to a significant milling force reduction.

4.3 Tool flank wear and subsurface deformation layer

High temperatures in cutting generally cause rapid tool wear, which in turn increases milling forces [18, 37]. In this study, tool flank wear was measured after each set

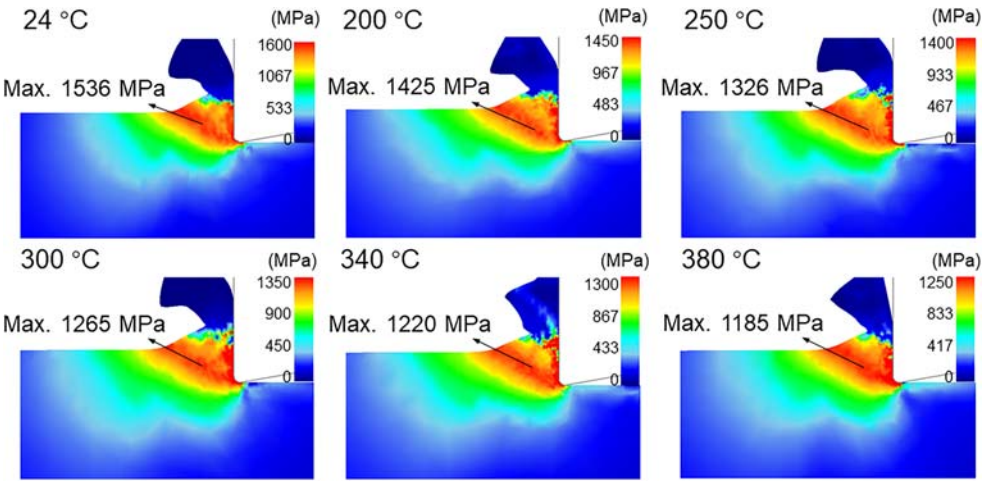

Fig. 10 Effective stress distribution in simulation when $f_z = 0.05$ mm/z

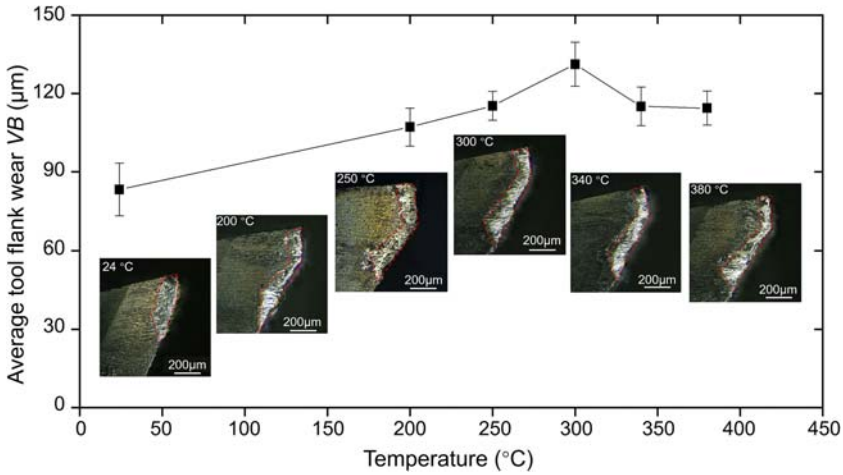

Fig. 11 Average tool flank wear at various preheating temperatures

of experiment. As shown in Fig. 11, the average tool flank wear was calculated based on $VB = A/a_p$, where A is flank wear area and a_p is the axial cutting depth. Tool flank wear reached the maximum VB of 130 μm at 300 °C at an increase of the preheating temperature, then decreased to around 115 μm as the preheating temperature continued to increase. As preheating temperature is lower than 300 °C, work hardening and high cutting temperature in the cutting zone contribute to the quick tool wear. At 340 °C and 380 °C, tool wear reduces due to dominant thermal softening effect.

The increase in tool flank wear is also one of the causes that increase the milling forces on the preheated workpieces. The milling force variation is reflected in the subsurface deformation layer, as shown in Fig. 12. At room temperature, subsurface deformation is hardly identified via the metallographic techniques. As the preheating temperature increases to 300 °C, the subsurface deformation layer thickness increases to around 4.9 μm at $f_z = 0.09$ mm/z. Tool flank wear is considered as one of the main factors leading to the increase in the subsurface deformation layer thickness [38–40]. However, as preheating temperature increases to 380 °C, the subsurface deformation layer thickness reaches the maximum of 5.9 μm even with a reduction in the tool flank wear, which may be due to the significant thermal softening effect of the workpiece material.

5 Conclusions

In this study, the characteristics of milling forces in ASHM of Ti-6Al-4V are investigated through a preheating milling experiment and a 2D thermal-mechanical coupling simulation model. The effect of temperature buildup on milling forces is investigated in combination with the analysis of cutting temperature and effective stress in simulation. The key conclusions are summarized.

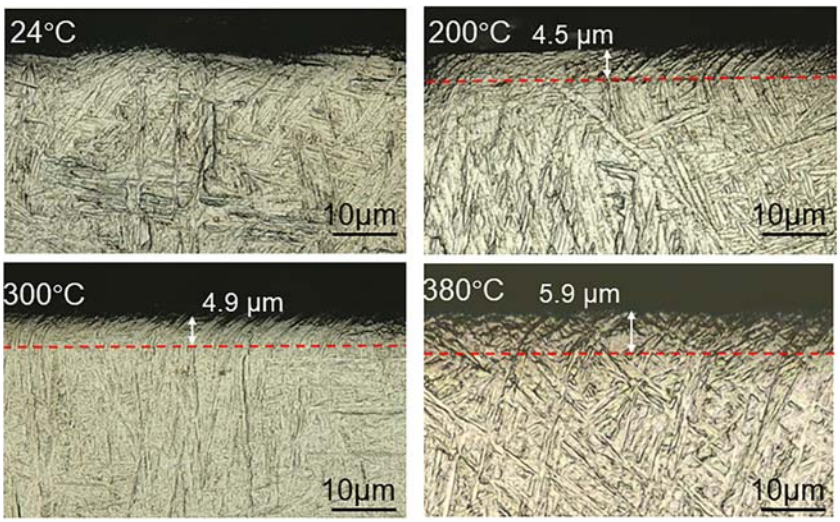

Fig. 12 Measurement of subsurface deformation layer thickness (polished cross-sections)

1. The range of temperature buildup is determined with the highest temperature of 380 °C after 20 s of deposition and 200 °C after 120 s.
2. The simulational milling forces are generally smaller than the measurement forces due to ignoring tool flank wear and the inaccurate material constitutive model. The peak forces are hardly decreased when preheating temperature is lower than 300 °C. A significant reduction of milling forces is found when preheating temperature is higher than 300 °C. F_{ymax} and F_{xmax} are decreased by 19.5% and 19.0% respectively at 380 °C when f_z is 0.05 mm/z. The decreasing trend is more obvious at a larger feed-per-tooth.
3. The thermal softening effect is the cause of the reduction in milling forces. Based on the simulation results, the cutting temperature increases with the preheating temperature, causing the reduction of material flow stress. However, as the preheating temperature is lower than 300 °C, the work hardening effect counteracts the thermal softening effect. With a further increase in the preheating temperature, an enhanced thermal softening effect causes a significant decrease in milling forces. At a larger feed-per-tooth, the thermal softening effect may overtake work hardening at a lower preheating temperature.
4. The fast increase in tool flank wear is also one of the causes of the unreduced milling forces at a preheating temperature lower than 300 °C. The thermal softening effect can be observed through the subsurface deformation layer thickness that increases with the preheating temperature.

Funding information The financial supports from the International cooperative research project of Shenzhen Science and Technology Innovation Commission (GJHZ20180411143506667) are gratefully acknowledged.

References

1. Nazir A, Abate KM, Kumar A, Jeng J-Y (2019) A state-of-the-art review on types, design, optimization, and additive manufacturing of cellular structures. Int J Adv Manuf Technol 104:1–22
2. Su X, Yang Y, Xiao D, Luo Z (2013) An investigation into direct fabrication of fine-structured components by selective laser melting. Int J Adv Manuf Technol 64(9–12):1231–1238
3. Kumar S, Sharma V, Choudhary AKS, Chattopadhyaya S, Hloch S (2013) Determination of layer thickness in direct metal deposition using dimensional analysis. Int J Adv Manuf Technol 67(9–12): 2681–2687
4. Soboyejo WO, Srivatsan TS (2006) Advanced structural materials: properties, design optimization, and applications. Scitech Book News, vol 2. CRC press, Boca Raton
5. Malekipour E, El-Mounayri H (2018) Common defects and contributing parameters in powder bed fusion AM process and their classification for online monitoring and control: a review. Int J Adv Manuf Technol 95(1–4):527–550
6. Zhang B, Li Y, Bai Q (2017) Defect formation mechanisms in selective laser melting: a review. Chin J Mech Eng 30(3):515–527
7. Flynn JM, Shokrani A, Newman ST, Dhokia V (2016) Hybrid additive and subtractive machine tools–research and industrial developments. Int J Mach Tool Manu 101:79–101
8. Du W, Bai Q, Wang Y, Zhang B (2018) Eddy current detection of subsurface defects for additive/subtractive hybrid manufacturing. Int J Adv Manuf Technol 95(9–12):3185–3195
9. Liu J, Wang X, Wang Y (2017) A complete study on satellite thruster structure (STS) manufactured by a hybrid manufacturing (HM) process with integration of additive and subtractive manufacture. Int J Adv Manuf Technol 92(9–12):4367–4377
10. Xiong X, Zhang H, Wang G (2009) Metal direct prototyping by using hybrid plasma deposition and milling. J Mater Process Technol 209(1):124–130
11. Ye ZP, Zhang ZJ, Jin X, Xiao MZ, Su JZ (2017) Study of hybrid additive manufacturing based on pulse laser wire depositing and milling. Int J Adv Manuf Technol 88(5–8):1–12
12. Du W, Bai Q, Zhang B (2016) A novel method for additive/subtractive hybrid manufacturing of metallic parts ☆. Procedia Manuf 5:1018–1030
13. Swarnakar AK, Biest OVD, Baufeld B (2011) Thermal expansion and lattice parameters of shaped metal deposited Ti–6Al–4V. J Alloys Compd 509(6):2723–2728
14. Ginta TL, Amin AKMN (2013) Thermally-assisted end milling of titanium alloy Ti-6Al-4V using induction heating. Int J Mach Mach Mater 14(2):194–212
15. Dandekar CR, Shin YC, Barnes J (2010) Machinability improvement of titanium alloy (Ti–6Al–4V) via LAM and hybrid machining. Int J Mach Tool Manu 50(2):174–182
16. Sun S, Brandt M, Dargusch MS (2010) Thermally enhanced machining of hard-to-machine materials—a review. Int J Mach Tool Manu 50(8):663–680
17. Sun S, Brandt M, Barnes JE, Dargusch MS (2011) Experimental investigation of cutting forces and tool wear during laser-assisted milling of Ti-6Al-4V alloy. P I Mech Eng B-J Eng 225(9):1512–1527
18. Rashidab RAR, Sun S, Wang G, Dargusch MS (2012) An investigation of cutting forces and cutting temperatures during laser-assisted machining of the Ti–6Cr–5Mo–5V–4Al beta titanium alloy. Int J Mach Tool Manu 63:58–69
19. Hedberg GK, Shin YC, Xu L (2015) Laser-assisted milling of Ti-6Al-4V with the consideration of surface integrity. Int J Adv Manuf Technol 79(9–12):1645–1658
20. Yang D, Liu Z, Ren X, Zhuang P (2016) Hybrid modeling with finite element and statistical methods for residual stress prediction in peripheral milling of titanium alloy Ti-6Al-4V. Int J Mech Sci 108:29–38
21. Dinda GP, Song L, Mazumder J (2008) Fabrication of Ti-6Al-4V scaffolds by direct metal deposition. Metall Mater Trans A 39(12): 2914–2922
22. Polishetty A, Shunmugavel M, Goldberg M, Littlefair G (2016) Singh RK (2016) cutting force and surface finish analysis of machining additive manufactured titanium alloy Ti-6Al-4V. Procedia Manufacturing 7:284–289
23. Milton S, Morandeau A, Chalon F, Leroy R (2016) Influence of finish machining on the surface integrity of Ti6Al4V produced by selective laser melting. Procedia CIRP 45:127–130
24. Bordin A, Bruschi S, Ghiotti A, Bucciotti F, Facchini L (2014) Comparison between wrought and EBM Ti6Al4V machinability characteristics. Key Eng Mater 611-612:1186–1193
25. Chen G, Ren C, Yang X, Jin X, Guo T (2011) Finite element simulation of high-speed machining of titanium alloy (Ti–6Al–4V) based on ductile failure model. Int J Adv Manuf Technol 56(9–12):1027–1038
26. Fahad M (2012) A heat partition investigation of multilayer coated carbide tools for high speed machining throughexperimental studies

and finite element modelling. The University of Manchester (United Kingdom), Manchester
27. Thepsonthi T, Özel T (2013) Experimental and finite element simulation based investigations on micro-milling Ti-6Al-4V titanium alloy: effects of cBN coating on tool wear. J Mater Process Technol 213(4):532–542
28. Ding H, Shen N, Shin YC (2012) Thermal and mechanical modeling analysis of laser-assisted micro-milling of difficult-to-machine alloys. J Mater Process Technol 212(3):601–613
29. Waldorf DJ (1996) Shearing, ploughing, and wear in orthogonal machining. University of Illinois, Urbana-Champaign
30. Hou Y, Zhang D, Wu B, Luo M (2014) Milling force modeling of worn tool and tool flank wear recognition in end milling. IEEE-ASME T Mech 20(3):1024–1035
31. Ducobu F, Arrazola PJ, Rivière-Lorphèvre E, Filippi E (2015) Finite element prediction of the tool wear influence in Ti6Al4V machining. Procedia CIRP 31:124–129
32. Zamani H, Hermani J-P, Sonderegger B, Sommitsch C (2013) 3D simulation and process optimization of laser assisted milling of Ti6Al4 V. Procedia CIRP 8:75–80
33. Deng WJ, Xia W, Tang Y (2009) Finite element simulation for burr formation near the exit of orthogonal cutting. Int J Adv Manuf Technol 43(9–10):1035
34. Wu YC (2014) FEM simulation of milling tool wear for titaninum alloys TC4. Shangdong University, Jinan
35. Seo S, Min O, Yang H (2005) Constitutive equation for Ti–6Al–4V at high temperatures measured using the SHPB technique. Int J Impact Eng 31(6):735–754
36. Parida AK, Maity K (2019) Hot machining of Ti–6Al–4V: FE analysis and experimental validation. Sādhanā 44(6):142
37. Bermingham M, Sim W, Kent D, Gardiner S, Dargusch M (2015) Tool life and wear mechanisms in laser assisted milling Ti–6Al–4V. Wear 322:151–163
38. Zhou JM, Bushlya V, Peng RL, Johansson S, Avdovic P, Stahl JE (2011) Effects of tool wear on subsurface deformation of nickel-based superalloy. Procedia Engineering 19(1):407–413
39. Liu CR, Barash MM (1976) The mechanical state of the sublayer of a surface generated by chip-removal process—part 2: cutting with a tool with flank wear. J Eng Ind 98(4):1202
40. Altintas Y, Ber AA (2001) Manufacturing automation: metal cutting mechanics, machine tool vibrations, and CNC design. Appl Mech Rev 54(5):B84